ELSEVIER

Design and modeling of a magnetic shock absorber based on eddy current damping effect

Babak Ebrahimi[a], Mir Behrad Khamesee[a],*, M. Farid Golnaraghi[b]

[a]*Department of Mechanical and Mechatronics Engineering, University of Waterloo, Waterloo, Ontario, Canada N2L 3G1*
[b]*Mechatronic Systems Engineering, Simon Fraser University, Surrey, British Columbia, Canada V3 T 0A3*

Abstract

This paper describes the design, modeling, and analysis of a novel magnetic spring–damper. This cost-effective, self-powered magnetic spring–damper utilizes two permanent magnets and a conductive aluminum plate to generate both spring and variable damping effects. Eddy currents are generated in the aluminum plate due to its relative motion with respect to the magnets. These eddy currents produce a repulsive force that is proportional to the velocity of the conductor such that the moving magnet and conductor act as a viscous damper. The structure of the proposed passive magnetic spring–damper is simple, and does not require an external power supply or any other electronic device. An accurate, analytical model of the system is obtained by using the electromagnetic theory to estimate the electromagnetic forces, induced in the system. The newly developed model can be used to design high-performance dampers for various applications. To optimize the design, simulations are conducted and the design parameters are evaluated. After a magnetic spring–damper prototype is fabricated, experiments are conducted to verify the accuracy of the theoretical model. The eddy current model exhibits a 7.5% RMS error for the damping ratio estimation, and a damping ratio as high as 40 N s/m is achieved by the fabricated prototype.

1. Introduction

Eddy currents are generated in a conductor in a time-varying magnetic field. They are induced either by the movement of the conductor in the static field or by changing the strength of the magnetic field, initiating motional and transformer electromotive forces (emfs), respectively. Since the generated eddy currents create a repulsive force that is proportional to the velocity of the conductor, the moving magnet and conductor behave like a viscous damper. Graves et al. [1] have derived a mathematical representation for eddy current dampers, based on the motional and transformer emf, and have developed an analytical approach to compare the efficiency of the dampers in terms of these two sources. For more than two decades, the application of eddy currents for damping purposes has been investigated, including magnetic braking systems [2–4], vibration

---

*Corresponding author. Tel.: +1 519 888 4567 35095.

E-mail address: khamesee@uwaterloo.ca (M.B. Khamesee).

Nomenclature

B	magnetic flux density	**M**	magnetization
		$\hat{\mathbf{n}}$	unit surface normal
$E(k)$	elliptic integral of the first kind	R	permanent magnet radius
F	force	t	time
g	gap between two magnets	V	induced electromotive force
I	electrical current	V_{emf}	motional electromotive force
$\mathbf{j}_m$	equivalent surface current density of a permanent magnet	V_{trans}	transformer electromotive force
		v	equivalent velocity of the aluminum plate
J	current density	$\hat{\mathbf{z}}$	longitudinal unit vector
$\mathbf{J}_m$	equivalent volume current density of a permanent magnet	Γ	conductor volume
		δ	conductor thickness
$K(k)$	elliptic integral of the second kind	μ_0	permeability of free space
L	length of the magnet	σ	conductivity
		$\hat{\boldsymbol{\varphi}}$	tangential unit vector

control of rotary machinery [5], structural vibration suppression [6–8], and vibration isolation enhancement in levitation systems [9,10].

Sodano et al. [6] have analyzed the suppression of cantilever beam vibrations, where a permanent magnet is fixed so that it is perpendicular to the beam motion, and a conducting sheet is attached to the beam tip. In Ref. [8], a theoretical model of an eddy current damper has been modified and further developed by applying an image method to satisfy the boundary condition of the zero eddy current density at the conducting plate's boundaries. An additional permanent magnet is included in the device with the like-poles fixed in the same direction, intensifying the radial magnetic flux density, enhancing the damping effect. Teshima et al. [9] have studied the effect of an eddy current damper on the vibration isolation properties of superconducting levitation, and demonstrated that in the vertical direction, the damping is improved by approximately 100 times by using eddy current dampers. Elbuken et al. [10] have investigated the eddy current damping for high precision magnetic levitation. The authors in Ref. [10] have suggested an eddy current damper to suppress the vibration of the levitated object. Karnopp [11] has devised a new electromechanical damper for vehicle applications, consisting of copper wire and permanent magnets. He has demonstrated that for oscillation frequencies, expected in road vehicle suspensions, electrodynamic variable shock absorbers are feasible. Schmid and Varaga [12] have designed and analyzed a vibration attenuation system for the construction of high-resolution nanotechnology structures such as the scanning tunnelling microscope by using eddy current dampers. For eddy current dampers and couplers under dynamic conditions, Tonoli [13] has presented a physical, dynamic model.

The application of the magnetic spring effect [14,15], and eddy current effect [6–8] in vibration suppression studies have been reported, but, to the best of the authors' knowledge, the application of eddy currents with a magnetic spring effect has not been addressed in prior publications. Magnetic spring dampers are appealing in various vibration isolation systems such as precision machinery, structure vibration isolation, and vehicle suspension systems.

In this article, the eddy current damping effect is exploited for the development of a spring–damper, and a model of the magnetic and eddy current forces for the designed magnetic spring–damper is proposed. Fig. 1 is a schematic of the proposed system, which consists of a ring-shaped conducting aluminum plate and two cylindrical permanent magnets, whose like-poles are in close proximity. The lower permanent magnet and the aluminum plate are stationary, while the upper magnet has a reciprocating motion. The use of a ring-shaped conductor plate simplifies the fabrication, and its thickness does not limit the magnets' air gap. Also, the conductor's shape is more appropriate for laboratory experiments that are described in Section 6.3. The relative movement of the magnets causes the conducting plate to undergo a time-varying magnetic field such that a transformer eddy current is generated. Since there is a relative movement between magnets and the conducting plate, a motional eddy current is generated as well.
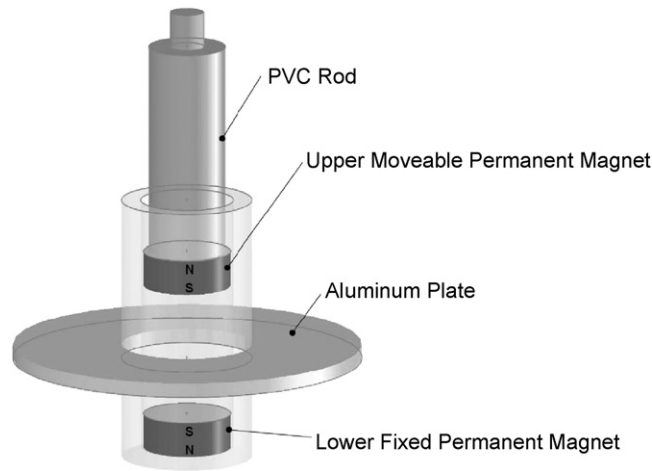
Fig. 1. Schematic view of the proposed eddy current spring–damper.

An analytical approach is adopted for modeling the proposed damper. Finite element modeling and the experimental results verify the accuracy of the analytical model, derived from basic electromagnetic principles. This paper outlines the steps to model the proposed magnetic spring–damper. First, the magnetic flux density, generated by a single cylindrical permanent magnet is calculated in Section 2 by the current method [16]. The calculated flux density is validated with finite element and experimental results, and then used for the eddy current calculation in Section 4. Next, the repulsive force between the two adjacent magnets is calculated, and the spring effect is characterized via combining the current method and Ampere's force law. In Section 6.2, the accuracy of the newly developed force model is confirmed by the finite element and experimental results. Finally, the motional eddy force and transformer eddy force are calculated and validated separately by experimental results that ultimately lead to the dynamic damping modeling and analysis of the designed magnetic spring–damper.

2. Magnetic flux density calculation

There are a number of approaches for calculating the magnetic flux density of a permanent magnet. The simplest approach is the dipole moment model, which is more appropriate for the flux density calculation for long distances, compared with the magnets' diameter. The charge method and the current method, model the magnet with a distribution of the charge and the current, respectively [16]. In this article, the current model is used for modeling the permanent magnets. Furlani [16] has shown that a cylindrical magnet can be replaced by an equivalent magnetic volume current density $\mathbf{J}_m = \nabla \times \mathbf{M}$ and an equivalent surface current density $\mathbf{j}_m = \mathbf{M} \times \hat{\mathbf{n}}$ that circulates around the body of the cylinder. $\mathbf{M}$ and $\hat{\mathbf{n}}$ are the magnetization vector and unit surface normal, respectively. By assuming that the cylindrical magnet is polarized along its longitudinal direction with unit vector $\hat{\mathbf{z}}$ and that a uniform magnetization, i.e., $\mathbf{M} = M\hat{\mathbf{z}}$, the volume and surface current densities are

$$\mathbf{J}_m = 0,$$
$$\mathbf{j}_m = M\hat{\boldsymbol{\varphi}}, \tag{1}$$

where $\hat{\boldsymbol{\varphi}}$ is the tangential unit vector. For a cylindrical current sheet, extending between $z' = \pm L/2$, the flux density components at (r, z) are given by Craik [17] as

$$B_r = \frac{\mu_0 I}{2\pi L} \int_{-L/2}^{L/2} \frac{(z - z')}{r[(R + r)^2 + (z - z')^2]^{1/2}} \left[-K(k) + \frac{R^2 + r^2 + (z - z')^2}{(R - r)^2 + (z - z')^2} E(k) \right] \mathrm{d}z',$$

$$B_z = \frac{\mu_0 I}{2\pi L} \int_{-L/2}^{L/2} \frac{1}{[(R + r)^2 + (z - z')^2]^{1/2}} \left[K(k) + \frac{R^2 - r^2 - (z - z')^2}{(R - r)^2 + (z - z')^2} E(k) \right] \mathrm{d}z', \tag{2}$$

where $K(k)$ and $E(k)$ are the complete elliptic integrals of the first and second kind, respectively, and are defined as

$$K(k) = \int_0^{\pi/2} \frac{\mathrm{d}\theta}{\sqrt{1 - k^2 \sin^2 \theta}} \tag{3}$$

and

$$E(k) = \int_0^{\pi/2} \sqrt{1 - k^2 \sin^2 \theta}\,\mathrm{d}\theta, \tag{4}$$

where

$$k^2 = 4Rr[(R+r)^2 + (z-z')^2]^{-1}.$$

Parameters R and L are the radius and length of the cylindrical permanent magnet, respectively, and $I = ML$ is the equivalent current of the permanent magnet [17]. Since Eq. (2) does not have any analytical solution [6], a numerical approach is used for solving the integrals. The estimated values are validated by the FE and experimental results. The calculated magnetic flux density is used for the estimation of the eddy current in Section 4.

3. Magnetic force calculation

In this section, the repulsion force between the two adjacent cylindrical permanent magnets is obtained by considering the magnets as two single current-carrying loops, and two solenoids, as depicted in Fig. 2. The force that a single current-carrying loop undergoes in the presence of another current-carrying loop is calculated by applying Ampere's force law. It states that when two current-carrying elements $I_1\,\mathrm{d}L1$ and $I_2\,\mathrm{d}L_2$ interact, the elemental magnetic force, exerted by element 1 on element 2, is

$$\mathrm{d}\mathbf{F}_{21} = \frac{\mu_0 I_2\,\mathrm{d}\mathbf{L}_2}{4\pi} \times \left[\frac{I_1\,\mathrm{d}\mathbf{L}_1 \times \mathbf{R}_{21}}{R_{21}^3} \right], \tag{5}$$

where $\mathbf{R}_{21}$ is the distance vector between the two elements, as illustrated in Fig. 2. R_1 and R_2 are the radii of loop one and two, respectively.

Therefore, the magnetic force is

$$\mathbf{F}_{21} = \frac{\mu_0}{4\pi} \int_{c2} I_2\,\mathrm{d}\mathbf{L}_2 \times \int_{c1} \frac{I_1\,\mathrm{d}\mathbf{L}_1 \times \mathbf{R}_{21}}{R_{21}^3}. \tag{6}$$
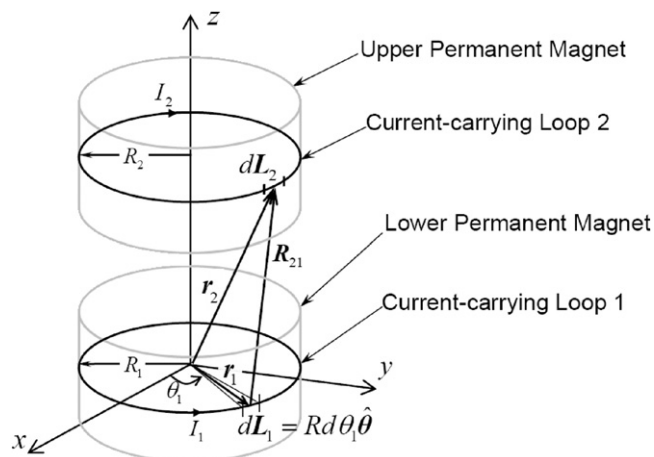

Fig. 2. Schematic of two current-carrying loops, illustrating the variables used in Eq. (5).

The right integral is the magnetic flux density produced by current-carrying loop 1 at the location of element 2. Typically, when a current-carrying loop is placed in an external magnetic field **B**, the magnetic force of the loop is mathematically expressed as

$$\mathbf{F} = \int_c I \, \mathrm{d}\mathbf{L} \times \mathbf{B}. \tag{7}$$

By assuming $R_1 = R_2 = R$, the vertical component of the interacting forces between two current-carrying loops with the opposite current direction is

$$F_z(z_d) = \frac{\mu_0 I_1 I_2 R^2}{4\pi} \int_0^{2\pi} \int_0^{2\pi} \frac{-z_d \cos(\theta_2 - \theta_1) \, \mathrm{d}\theta_1 \, \mathrm{d}\theta_2}{(2R^2 - 2R^2 \cos(\theta_2 - \theta_1) + z_d^2)^{3/2}}, \tag{8}$$

where z_d is the distance between the two loops. By using the same current technique as that for the permanent magnet modeling, the vertical component of the interacting forces between the two adjacent magnets with the opposite magnetization direction is obtained by integrating Eq. (8) along the magnets' length as follows:

$$F_z = \frac{\mu_0 I_1 I_2 R^2}{4\pi L^2} \int_{g/2}^{g/2+L} \int_{-L-g/2}^{-g/2} \int_0^{2\pi} \int_0^{2\pi} \frac{-[z_d - z' - z''] \cos(\theta_2 - \theta_1) \, \mathrm{d}\theta_1 \, \mathrm{d}\theta_2 \, \mathrm{d}z' \, \mathrm{d}z''}{(2R^2 - 2R^2 \cos(\theta_2 - \theta_1) + [z_d - z' - z'']^2)^{3/2}}. \tag{9}$$

Eqs. (8) and (9) are used in Section 6.2 as alternative approaches for the magnetic force estimation. It is seen that the single-loop approximation of Eq. (8) maintains its accuracy for the wide air gap between the magnets, but underestimates the magnetic force for the narrower air gaps. The accuracy of the calculated repulsive force in Eq. (9) is verified in Section 6.2 by using the finite element and experimental results. Finally, Eq. (9) is used to anticipate the spring behavior of the magnetic spring–damper device.

4. Eddy current damping force

Fig. 3 exhibits the configuration of the eddy current damping system, where the stationary aluminum plate is the source of the eddy currents due to the movement of the upper permanent magnet.

Fig. 4 demonstrates a two-dimensional (2D) axial-symmetry finite element model of the proposed system. The streamlines represent the magnetic flux density. The upper magnet in Fig. 4(b) is moved 10 mm closer to the lower magnet, compared with Fig. 4(a). This movement is equivalent to moving the aluminum plate with a thickness of δ and a conductivity of σ up 5 mm. It is noteworthy that the plate velocity (v) should be considered as half of the upper magnets' velocity.

As shown in Fig. 4, permanent magnets generate a time-varying magnetic field in both the axial (z) and radial (r) directions. The total generated emf of the aluminum plate is based on either a time-varying magnetic field, or the relative motion of the conducting plate. The former contribution is associated with the
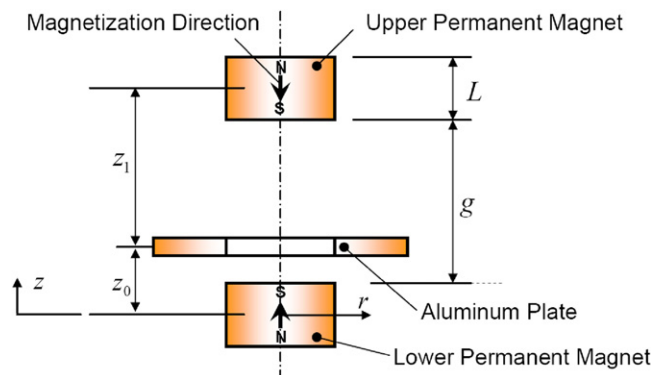

Fig. 3. Geometric definition of the eddy current spring–damper.

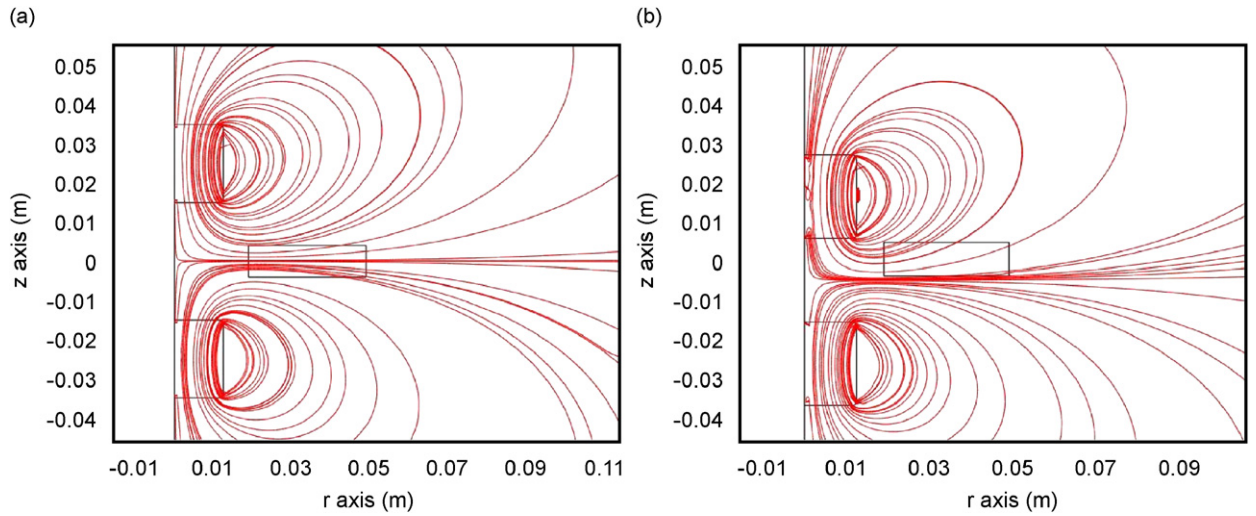(a)   (b)

Fig. 4. 2D axial-symmetry Femlab simulation of the system, where the air gap is decreased from (a) 30 mm to (b) 20 mm; the streamlines represent the magnetic flux density (other specifications are listed in Table 1).

"transformer emf" and is easily obtained from the third Maxwell equation (Faraday's law), whereas the latter is associated with the "motional emf" and is derived from the Lorentz force law by calculating

$$V = V_{\text{trans}} + V_{\text{motional}} = -\int_s \frac{\partial \mathbf{B}}{\partial t} \cdot d\mathbf{s} + \int_c (\mathbf{v} \times \mathbf{B}) \cdot d\mathbf{l}. \tag{10}$$

Also, it is noted that plate velocity (v) is actually the relative velocity of the conducting plate with respect to the permanent magnets. Since the movement of the aluminum plate is in the vertical direction, the vertical component of the magnetic flux density does not contribute to the generation of the motional eddy current (i.e., $\mathbf{v} \times \mathbf{B}_z = 0$). As a result, the generated motional-emf depends on the radial component of the magnetic flux density. The current density $\mathbf{J}$, induced in the conducting sheet due to the motional emf is

$$\mathbf{J} = \sigma(v \times \mathbf{B}). \tag{11}$$

The damping force due to the motional emf term is defined [6] by computing

$$\mathbf{F}_{\text{motional}} = \int_\Gamma \mathbf{J} \times \mathbf{B} \, d\Gamma = -\hat{\mathbf{k}}\sigma\delta v \int_0^{2\pi} \int_{r_{\text{in}}}^{r_{\text{out}}} r B_r^2(r, z_0) \, dr \, d\theta, \tag{12}$$

where Γ is the conductor volume. As demonstrated in Fig. 3, the total radial component of the magnetic flux density is the sum of the magnetic flux density, generated by the two permanent magnets at the mid-plane of the conducting plate such that

$$B_{r,\text{total}} = B_r(z_0) + B_r(z_1), \tag{13}$$

where

$$z_1 = \begin{vmatrix} L + g - z_0 & \text{if } z_0 < L + g, \\ -L - g + z_0 & \text{if } z_0 > L + g. \end{vmatrix}$$

Eq. (12) is valid for only an infinite conducting plate, indicating that the boundary condition of zero current at the conducting plate's boundaries (the edge effect) is not considered. If the edge effect is not considered, the predicted force is overestimated [8]. To include the edge effect, the image method [18] is employed, as
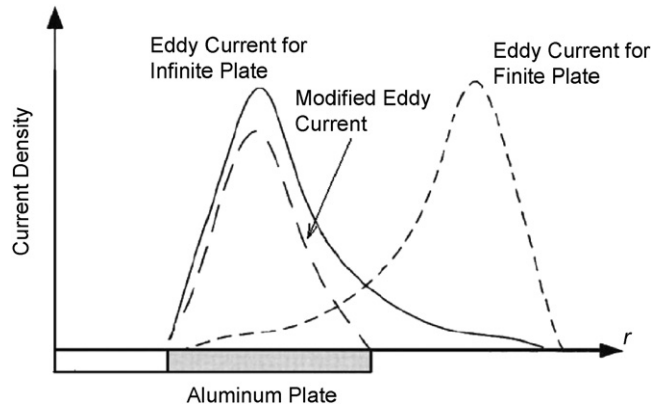
Fig. 5. Modification of the eddy current using the image method [8].

illustrated in Fig. 5. Thus, the motional eddy current force is modified by calculating

$$\mathbf{F}_{\text{motional}} = -\hat{\mathbf{k}}\sigma\delta v\left(\int_0^{2\pi}\int_{r_{\text{in}}}^{r_{\text{out}}} rB_r^2(r,z_0)\,\mathrm{d}r\,\mathrm{d}\theta - \int_0^{2\pi}\int_{r_{\text{in}}}^{r_{\text{out}}} rB_r^2(2r_{\text{out}}-r,z_0)\,\mathrm{d}r\,\mathrm{d}\theta\right)$$
$$= -\hat{\mathbf{k}}\sigma 2\pi\delta v\left(\int_{r_{\text{in}}}^{r_{\text{out}}} rB_r^2(r,z_0)\,\mathrm{d}r - \int_{r_{\text{in}}}^{r_{\text{out}}} rB_r^2(2r_{\text{out}}-r,z_0)\,\mathrm{d}r\right). \tag{14}$$

As denoted in Fig. 5, the first term in Eq. (14) corresponds to the damping force to account for the infinite plate, whereas the second term is the damping force for considering the imaginary eddy currents. The subtraction of these two terms gives the modified motional damping force. Since the magnetic field is not uniform in the vertical direction, the aluminum plate is prone to a magnetic flux density variation during the reciprocating oscillation. Consequently, the transformer term should be considered in the eddy current calculations.

The transformer emf is calculated by conducting numerical integration over the surface of the conductor plate as follows:

$$V_{\text{trans}} = -\int_s \frac{\partial\mathbf{B}}{\partial t}\cdot\mathrm{d}\mathbf{s} = -\int_s\left(\frac{\partial\mathbf{B}}{\partial z}\frac{\partial z}{\partial t}+\frac{\partial\mathbf{B}}{\partial r}\frac{\partial r}{\partial t}\right)\cdot\mathrm{d}\mathbf{s} = -\int_s\left(\frac{\partial\mathbf{B}_z}{\partial z}\frac{\partial z}{\partial t}\hat{z}+\frac{\partial\mathbf{B}_r}{\partial z}\frac{\partial z}{\partial t}\hat{r}\right)\cdot\mathrm{d}\mathbf{s}, \tag{15}$$

where the second term in the last integral is zero, by considering the symmetry of the radial flux density about the plate center axis. The calculated gradient of the magnetic flux density on the bottom surface is reduced from that of the upper one, since their respective normal units are in the opposite directions. Therefore, the damping force generated by the transformer eddy currents, is calculated from the respective emf (V_{trans}) as follows:

$$\mathbf{F}_{\text{trans}} = \frac{-\mathbf{k}\sigma}{l}\int_s \frac{\partial\mathbf{B}}{\partial t}\,\mathrm{d}\mathbf{s}\int rB_r\,\mathrm{d}\Gamma = \frac{-\mathbf{k}\sigma v}{l}\int_s \frac{\partial B_z}{\partial z}\,\mathrm{d}\mathbf{s}\int rB_r\,\mathrm{d}\Gamma \tag{16}$$

in which $l = \pi(r_{\text{out}}+r_{\text{in}})$.

Thus, Eqs. (14) and (16) provide the motional and transformer damping force estimation, and the total damping force is validated in Section 6.3 by some experimental results.

5. Experimental setup

Two experimental setups are established to validate the accuracy of the three developed models in Sections 2–4. The magnetic spring–damper in Fig. 1 is fabricated and tested, as shown in Figs. 6 and 7. The physical properties of the newly developed prototype are listed in Table 1. The permanent magnets in this experiment are neodymium–iron–boron rare-earth magnets with a radius of 25 and length of 20 mm.
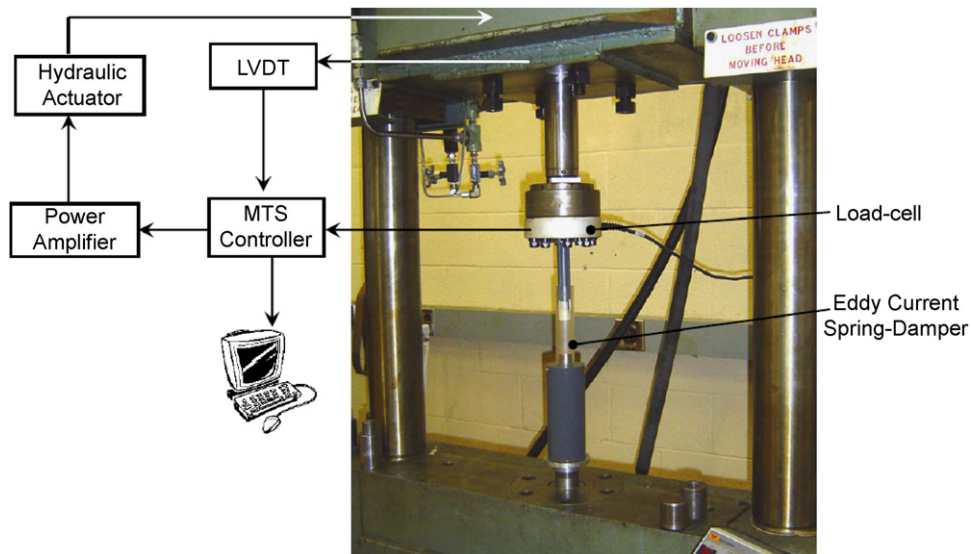
Fig. 6. First experimental test bed for large amplitudes and low frequencies.
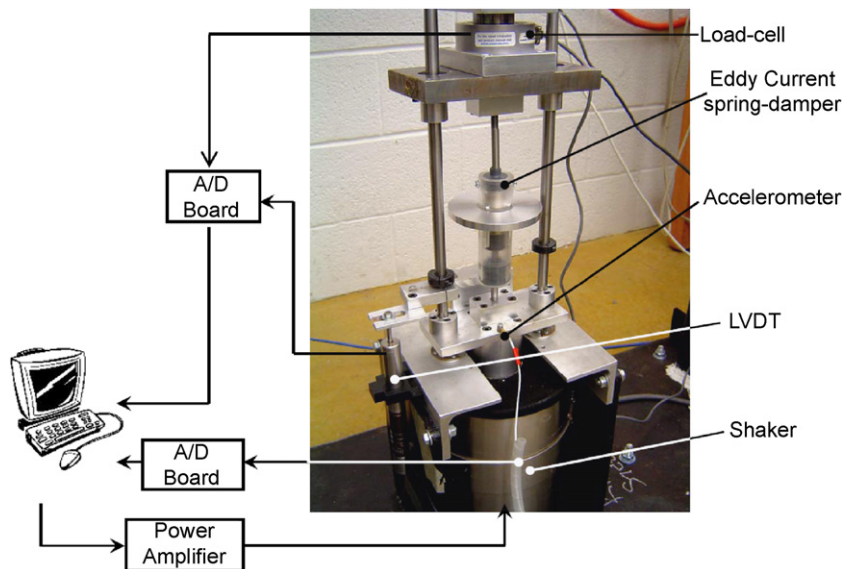

Fig. 7. Second experimental test bed for small amplitudes and high frequencies.

The prototype frame, as well as the rod connecting the upper permanent magnet to the load cell, is composed of PVC to avoid interference with the magnetic field. The first test bed in this experiment is composed of a hydraulic actuator with feedback from an LVDT displacement sensor, a 1 klb load cell and an MTS-FlexTest-SE controller device. This system is particularly appropriate for large displacement strokes (more then 5 mm) and static force measurements. The hydraulic shaker covers the frequencies as high as 5 Hz at a 15 mm displacement amplitude. Fig. 6 reflects the first experimental test bed to verify the spring effect of the magnetic spring–damper.

As seen in Fig. 7, the second experimental test bed is prepared, achieving higher accuracies for small amplitudes and high frequencies. The setup consists of an electromagnetic shaker, which is controlled by accelerometer sensor feedback data. Load-cell data, as well as LVDT displacement data, is captured by another A/D board. The electromagnetic shaker is capable of producing amplitudes up to 3 mm and a force up to 100 lbf. All of the measurements are carried out at the University of Waterloo.

Table 1
Physical properties of the experimental configuration

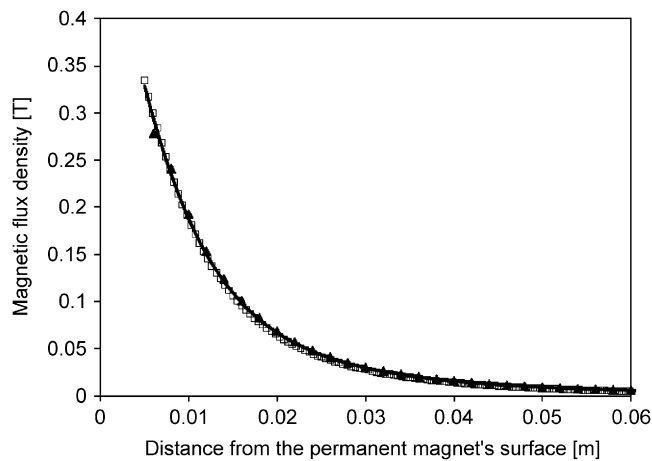| Property	Value
Aluminum electrical conductivity	3.37e7 (S/m)
Inside diameter of aluminum plate	38 (mm)
Outside diameter of aluminum plate	100 (mm)
Thickness of the aluminum plate	8 (mm)
Permanent magnet diameter	25 (mm)
Permanent magnet length	20 (mm)
Magnetization of the permanent magnet	1.03e6 (A/m)
Permanent magnet composition	NdFeB42

Fig. 8. Vertical component of the magnetic flux density along the magnet's centerline. □: finite element results, ▬: theoretical results, ▲: experimental results.

6. Comparison of the mathematical model with the experimental results

In the experimental setups, the accuracy of the proposed model is verified. Before the eddy current damping force is established, the magnetic flux density and the force, generated by the permanent magnets, are calculated and verified by experimental results.

6.1. Verification of the magnetic field model

Since Eq. (2) does not have an analytical solution [6], it is numerically integrated. Fig. 8 shows the verification of the vertical component of the magnetic flux density along the magnet's centerline with the experimental results and the finite element results, obtained from Femlab 3.2 software. For the finite element results, the Lagrange-quadratic elements are used. The proposed model is reliable and is used for the eddy current estimation in Section 6.3.

6.2. Verification of the permanent magnets' interaction force model

The force equations for both the single-loop approximation (8) and solenoid electromagnet approximation (9) for simulating the permanent magnets are derived. Fig. 9 gives the results of these two approximations, compared with the finite element results. It is observed in Fig. 9 that the single current-carrying-loop method (8), in which the permanent magnet is modeled as a single current-carrying loop at the middle of the magnet's length, deviates from the solenoid approach (9) and the finite element results for the air gap between the
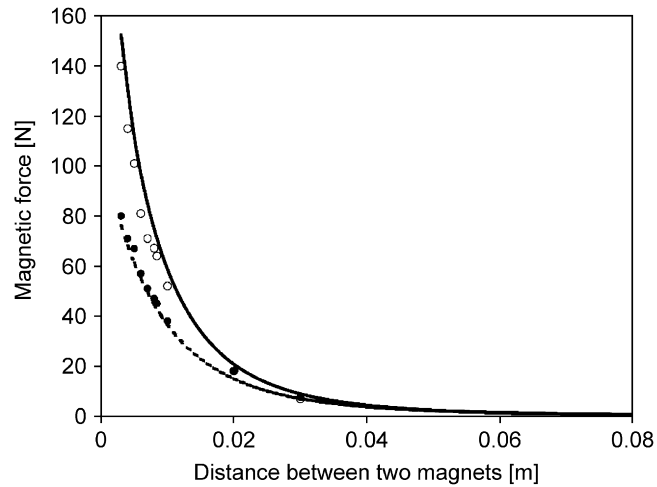
Fig. 9. Analytical and finite element results comparison for the interaction force between two magnets. — —: Analytical solution for a single loop, ——: analytical solution for a solenoid, ●: finite element solution for a single loop, ○: finite element solution for permanent magnet.
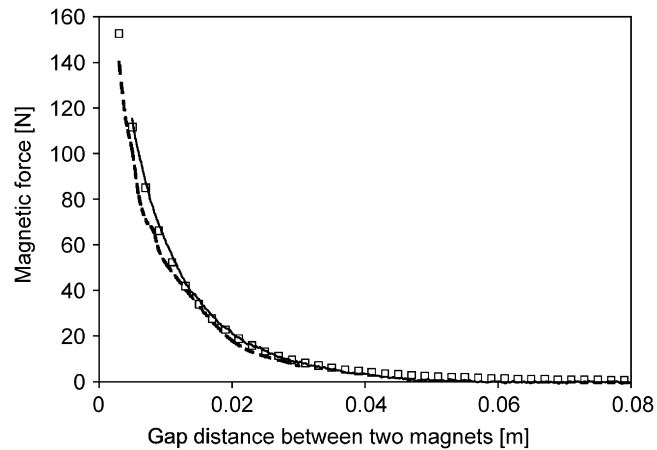

Fig. 10. Comparison of the experimental results and the analytical results. ——: Experimental force, □: analytical solution for a solenoid, ▬ ▬: finite element solution for permanent magnet.

magnets below 3 cm. It is revealed that modeling the permanent magnet with a single current-carrying loop is no longer valid for narrow gap distances between the magnets.

By using the first test setup in Fig. 6, the magnetic force between the two adjacent permanent magnets is experimentally measured. Fig. 10 signifies the accuracy of the proposed model, compared with the experimental results. Also, it is observed that a force, as high as 150 N can be achieved when the magnets' air gap is close to 5 mm. This graph also conveys the nonlinear spring characteristic of the system in the absence of the aluminum plate.

6.3. Validation of eddy current model

There are a number of factors that can affect the damping ratio, and they can be varied to attain the desirable damping characteristics. In this section, the effect of the air gap between the magnets, aluminum plate size, and position are considered. As mentioned in Section 4, the time-varying magnetic field, and the relative motion of the aluminum plate and permanent magnets produce two different effects, causing the
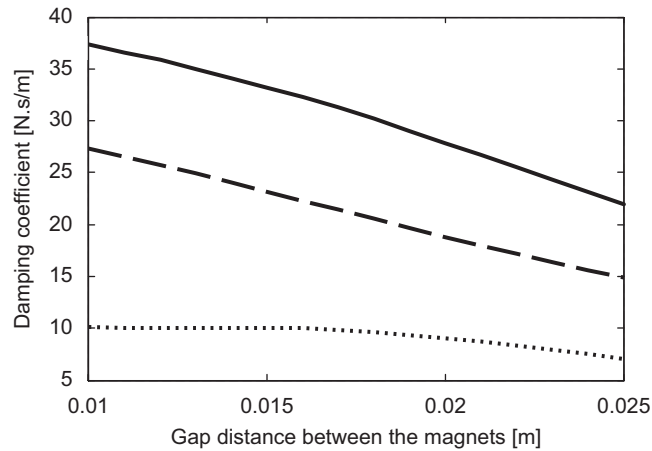
Fig. 11. Transformer, motional and total eddy current damping vs. distance between the magnets, where aluminum plate is located at mid-distance of the magnets and the upper magnet peak velocity is 0.3 m/s. ▬ ▬: Motional eddy current effect, ▪ ▪ ▪: transformer eddy current effect, ▬▬▬: total effect.
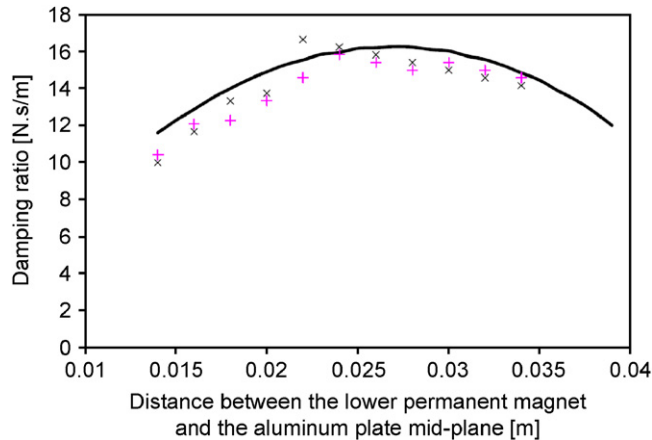

Fig. 12. Maximum eddy force at different conductor sheet positions, where the upper magnet peak velocity is 0.25 m/s and magnets gap is 30 mm. ✖: Experimental result 1, ➕: experimental result 2, ▬▬▬: analytical result.

opposing eddy force. Fig. 11 denotes the motional and transformer effects, contributing in the damping generation at the different size air gaps between the magnets. It is observed that for a vibration amplitude equal to 5 mm, the transformer eddy current contribution is 25% less than that of the motional eddy currents. This contribution varies in relation to the position and thickness of the aluminum plate. The plate is positioned in the middle of the air gap between the magnets in Fig. 11. The amplitude and frequency of the upper magnet oscillation are 5 mm and 10 Hz, respectively.

As illustrated in Fig. 11, the total damping effect decreases for the wider air-gap distance between the two magnets. Consequently, the desired damping ratio is achieved by choosing the gap distance between the magnets. The opposing eddy force, generated by eddy current effect, is also calculated for the different plate positions. Fig. 12 shows the analytical and experimental values for the damping coefficient at different aluminum plate positions (z_0), when the upper magnet peak velocity is 0.25 m/s and the air gap between the magnets is 30 mm. The aluminum plate positions are measured from the mid-plane of the lower permanent magnet.

It is observed that the most effective position for the aluminum plate is midway between the two permanent magnets. A comparison of the two sets of experiments with the analytical solutions shows an RMS error of
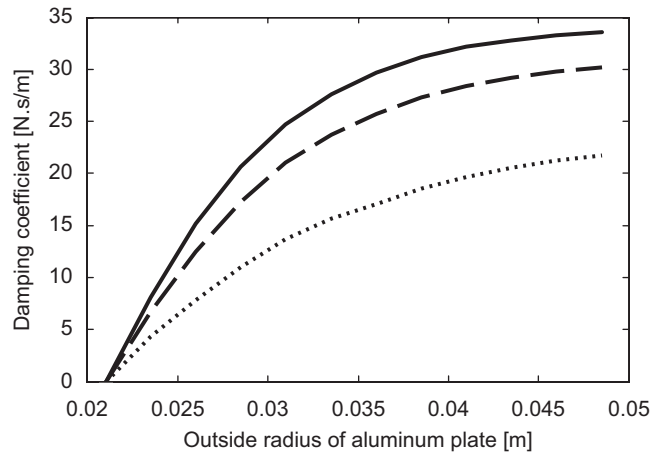
Fig. 13. Damping coefficient vs. outside radius of the aluminum plate, where the magnets' gap is 20 mm, and the upper magnet peak velocity is 0.3 m/s. ▬▬:$z_0 = 0.014$, ▬ ▬: $z_0 = 0.018$, ▪ ▪ ▪: $z_0 = 0.02$.
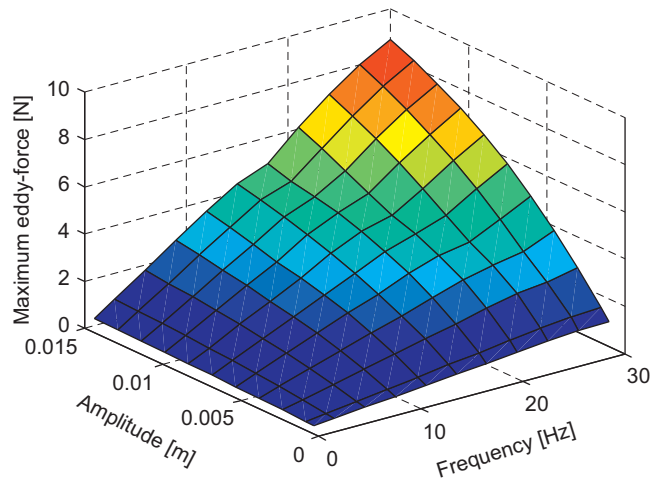

Fig. 14. Maximum eddy force at different vibration frequencies and amplitudes.

1.05 kg/s (7.5%) in the damping coefficient estimation. The slight peak-value offset in the analytical results can be due to the round-off error in the numerical calculation of integrals in Eq. (2).

The size of the conducting plate is optimized as exhibited in Fig. 13. It is observed that increasing the outside radius of the aluminum plate does not affect the damping coefficient after a certain level and so there is an optimal outside radius for each case to obtain the maximum damping coefficient. This figure is obtained for a 20 mm gap between the magnets, and the upper magnet oscillation amplitude and frequency are 5 mm and 10 Hz, respectively. Each line represents the specific aluminum plate position (z_0), measuring from the mid-plane of the lower magnet.

Fig. 14 signifies the maximum value of the eddy current's opposing force at different frequencies and amplitudes. It is observed that the damping characteristic of the eddy currents is similar to the linear viscous damper for the range of frequencies and amplitudes in Fig. 14. Also, the linear dependency of the force on the frequency at a low speed is confirmed in Ref. [19]. In addition, it is shown that a maximum damping force up to 10 N is achievable by using the specified dimensions. Figs. 13 and 14 illustrate the analytical results of Eqs. (14) and (16).

6.4. Dynamic damping characterization

The goal in this section is to derive an experimental non-parametric model of the magnetic spring–damper damping effect. By changing the prototype configuration, the damping effect can be distinguished from the spring effect. The damping characteristic is obtained separately; i.e., the magnetic spring–damper converts to a magnetic damper. The new test configuration comprises two fixed permanent magnets and a moving aluminum plate. Fig. 15 represents the dynamic behavior of the magnetic damper at three different frequencies. The fixed air gap between the magnets is set to 35 mm.

The experimental data proves the existence of the eddy current hysteresis effect. Several models have been proposed to represent the hysteresis phenomena. The Bouc–Wen model [20], as shown in Fig. 16, is one of the differential hysteresis models, which is used to model the eddy current hysteresis effect. The Bouc–Wen model has attracted more interest in the last few years due to the ease of its numerical implementation and ability to represent a wide range of hysteresis loop shapes [21]. In this model, the damping force is given by

$$F_{damper} = c\dot{x} + z, \tag{17}$$

where z is the force determined by computing the following:

$$\dot{z} = A\dot{x} - \beta|\dot{x}||z|^{n-1} - \gamma\dot{x}|z|^n, \tag{18}$$

where A, β, γ, c, and n are the experimental model's parameters, estimated by the nonlinear least square optimization method. The Bouc–Wen model parameters are $[c, \beta, \gamma, A, n] = [1.11, -50, 24, -69.5, 2]$.

Another important plot in the dynamic damper characterization is the peak force in terms of the peak velocity, which is obtained experimentally for a 35 mm air gap between the magnets and is given in Fig. 17. This plot confirms the linear damping properties of the eddy current effect, obtained in Eqs. (14) and (16).
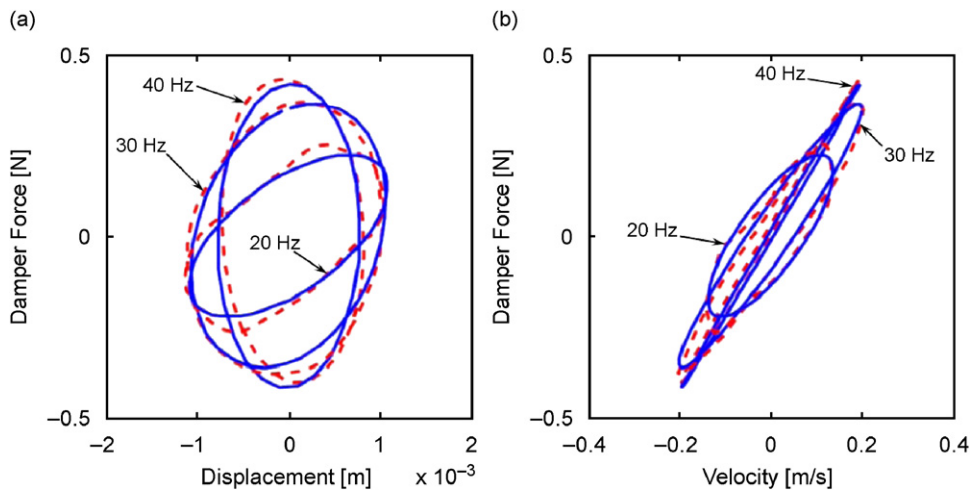

Fig. 15. Dynamic characterization of the MD: (a) force vs. displacement and (b) force vs. velocity. ▬ ▬: Experimental results, ▬▬: modeling.
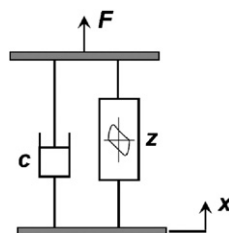

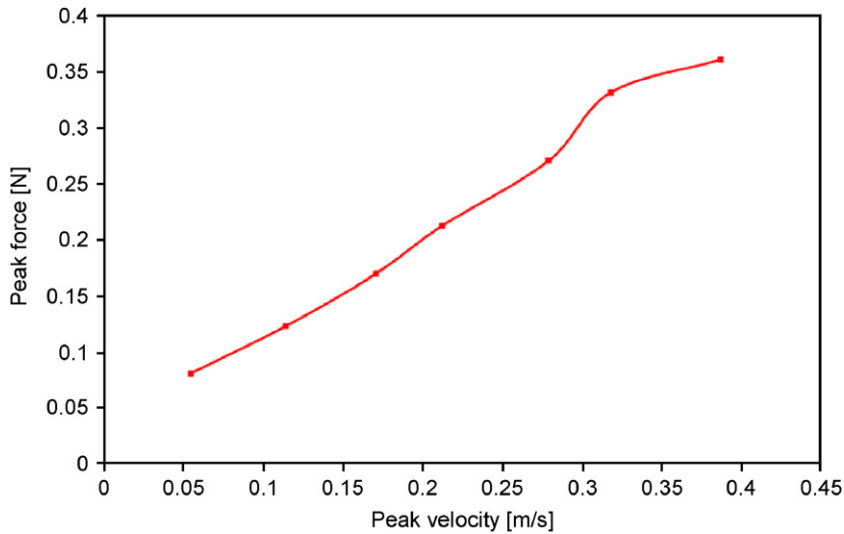Fig. 16. The Bouc–Wen model of the system.

Fig. 17. Peak force vs. peak velocity at a constant frequency of 20 Hz.

7. Conclusion

In this paper, a passive magnetic spring–damper system is developed by using the eddy current damping effect. The proposed magnetic spring–damper utilizes two permanent magnets and a stationary conductive aluminum plate. A theoretical model of the proposed system is constructed by using the transformer eddy current contribution and the image method for the motional eddy current estimation. The magnetic flux, interaction force of the magnets, and eddy current damping force are analytically calculated and validated by finite element and experimental results. Finally, the dynamic damping characterization of the system is derived by using the differential Bouc–Wen model.

The newly developed analytical model is used to design high-performance dampers for a variety of applications. The damping characteristic of the proposed system can be easily changed by either re-positioning the conductor or choosing the appropriate conductor size and the air-gap distance between the magnets. The novel magnetic spring–damper described in this article is a non-contact device with adjustable damping characteristics, no external power supply requirement, and suitable for different vibrational structures for high accuracy and simple implementation. The proposed magnetic spring–damper can be modified in terms of size, material, and topological design for different applications. Future work might involve extending the magnetic spring–damper design for vehicle suspension systems, since the damper is oil free, inexpensive, requires no external power, and is simple to manufacture.

Appendix A. Derivation of Eq. (8)

Regarding Fig. 2,

$$r_1 = R_1\hat{\mathbf{r}} + \theta_1\hat{\boldsymbol{\theta}} = R_1 \cos\theta_1\hat{\mathbf{i}} + R_1 \sin\theta_1\hat{\mathbf{j}}, \tag{A.1}$$

$$r_2 = R_2\hat{\mathbf{r}} + \theta_2\hat{\boldsymbol{\theta}} = R_2 \cos\theta_2\hat{\mathbf{i}} + R_2 \sin\theta_2\hat{\mathbf{j}} + z_d\hat{\mathbf{k}}, \tag{A.2}$$

$$\mathbf{R}_{21} = (-R_1 \cos \theta_1 + R_2 \cos \theta_2)\hat{\mathbf{i}} + (-R_1 \sin \theta_1 + R_2 \sin \theta_2)\hat{\mathbf{j}} + z_d\hat{\mathbf{k}}, \tag{A.3}$$

$$R_{21} = \sqrt{R_2^2 + R_1^2 - 2R_1R_2 \cos(\theta_2 - \theta_1) + z_d^2} \tag{A.4}$$

and

$$d\mathbf{L}_k = R_k \, d\theta_k \hat{\boldsymbol{\theta}} = -R_k \sin \theta_k \, d\theta_k \hat{\mathbf{i}} + R_k \cos \theta_k \, d\theta_k \hat{\mathbf{j}} \quad (k = 1, 2). \tag{A.5}$$

By assuming $R_1 = R_2 = R$, Ampere's force law results in

$$
\begin{aligned}
\boldsymbol{F}_{21} = \frac{\mu_0 I_1 I_2 R^2}{4\pi} \Big[& \int_0^{2\pi} \int_0^{2\pi} \frac{R \cos \theta_2 (1 - \cos(\theta_2 - \theta_1)) \, d\theta_1 \, d\theta_2}{(2R^2 - 2R^2 \cos(\theta_2 - \theta_1) + z_d^2)^{3/2}} \hat{\mathbf{i}} \\
& + \int_0^{2\pi} \int_0^{2\pi} \frac{R \sin \theta_2 (1 - \cos(\theta_2 - \theta_1)) \, d\theta_1 \, d\theta_2}{(2R^2 - 2R^2 \cos(\theta_2 - \theta_1) + z_d^2)^{3/2}} \hat{\mathbf{j}} \\
& + \int_0^{2\pi} \int_0^{2\pi} \frac{-z_d \cos(\theta_2 - \theta_1) \, d\theta_1 \, d\theta_2}{(2R^2 - 2R^2 \cos(\theta_2 - \theta_1) + z_d^2)^{3/2}} \hat{\mathbf{k}} \Big].
\end{aligned}
\tag{A.6}
$$

References

[1] K.E. Graves, D. Toncich, P.G. Iovenitti, Theoretical comparison of motional and transformer EMF device damping efficiency, *Journal of Sound and Vibration* 233 (2000) 441–453.

[2] L.H. Cadwell, Magnetic damping analysis of an eddy current brake using an airtrack, *American Journal of Physics* 64 (1996) 917–923.

[3] M.A. Heald, Magnetic braking: improved theory, *American Journal of Physics* 56 (6) (1996) 521–522.

[4] H.H. Wiederick, N. Gauthier, D.A. Campbell, P. Rochon, Magnetic braking: simple theory and experiment, *American Journal of Physics* 55 (6) (1987) 500–503.

[5] G. Genta, C. Delprete, A. Tonoli, E. Rava, L. Mazzocchetti, Analytical and experimental investigation of a magnetic radial passive damper, *Proceeding of the Third International Symposium of Magnetic Bearings*, Washington, DC, July 1992, pp. 255–264.

[6] H. Sodano, J.S. Bae, D.J. Inman, W.K. Belvin, Concept and model of eddy current damper for vibration suppression of a beam, *Journal of Sound and Vibration* 288 (2005) 1177–1196.

[7] J.S. Bae, M.K. Kwak, D.J. Inman, Vibration suppression of cantilever beam using eddy current damper, *Journal of Sound and Vibration* 284 (2005) 805–824.

[8] H. Sodano, J.S. Bae, D.J. Inman, W.K. Belvin, Improved concept and model of eddy current damper, *Transaction of the ASME* 128 (2006).

[9] H. Teshima, M. Tanaka, K. Miyamoto, K. Nohguchi, K. Hinata, Effect of eddy current dampers on the vibration properties in superconducting levitation using melt-processed YbaCuO bulk superconductors, *Physica C* 274 (1997) 17–23.

[10] C. Elbuken, M.B. Khamesee, M. Yavuz, Eddy current damping for magnetic levitation: downscaling from macro to micro-levitation, *Journal of Physics D: Applied Physics* 39 (2006) 3932–3938.

[11] D. Karnopp, Permanent magnet linear motors used as variable mechanical dampers for vehicle suspensions, *Journal of Vehicle System Dynamics* 18 (1989) 187–200.

[12] M. Schmid, P. Varga, Analysis of vibration-isolating systems for scanning tunnelling microscopes, *Ultramicroscopy* 42–44 (Part B) (1992) 1610–1615.

[13] A. Tonoli, Dynamic characteristics of eddy current dampers and couplers, *Journal of Sound and Vibration* 301 (2007) 576–591.

[14] P.J. Patt, Design and testing of a coaxial linear magnetic spring with integral linear motor, *IEEE Transactions on Magnetics* 21 (5) (1985) 1759–1761.

[15] K. Nagaya, M. Sugiura, A method for obtaining a linear spring for a permanent magnet levitation system using electromagnetic control, *IEEE Transactions on Magnetics* 13 (3) (1995) 2332–2338.

[16] E.P. Furlani, *Permanent Magnet and Electromechanical Devices, Materials, Analysis and Applications*, Academic Press, San Diego, 2001, pp. 126–130.

[17] D. Craik, *Magnetism, Principles and Applications*, Wiley, West Sussex, 1995, pp. 334–336.

[18] K. Lee, K. Park, Modeling eddy currents with boundary conditions by using Coulombs law and the method of images, *IEEE Transactions on Magnetics* 38 (2) (2002) 1333–1340.

[19] A. Canova, B. Vusini, Design of axial eddy current couplers, *IEEE Transactions on Industry Applications* 39 (3) (2003) 725–733.

[20] Y.K. Wen, M. Asce, Method of random vibration of hysteretic system, *Journal of Engineering Mechanics Division—ASCE* 102 (2) (1976) 249–263.

[21] F. Ikhouane, Vibration of the hysteresis loop with the Bouc–Wen model parameters, *Nonlinear Dynamics* 48 (4) (2007) 361–380.